J. Fluid Mech. (2001), *vol.* 446, *pp.* 199–228.
DOI: 10.1017/S0022112001005717 Printed in the United Kingdom

Evidence of longitudinal vortices evolved from distorted wakes in a turbine passage

By XIAOHUA WU AND PAUL A. DURBIN

Center for Integrated Turbulence Simulation, and Department of Mechanical Engineering, Stanford University, Building 500, Stanford, CA 94305-3030, USA

(Received 4 January 2000 and in revised form 6 May 2001)

Two types of longitudinal vortices are found to arise from distorted, migrating wakes convecting through a low-pressure turbine stator passage. The primary vortices emerge within the free stream as the wake is subjected to irrotational strains. Their axes align approximately with the local mean wake velocity. They are dragged over the surface and induce secondary vortices near the wall, which have the opposite sense of rotation to the primary vortices. Although they form on the concave side, these secondary vortices are neither produced, nor sustained by Görtler instability; rather, they are a consequence of severely straining the passing wakes.

Evidence is drawn from a numerical simulation of the unsteady, incompressible flow through a turbine stator passage with and without upstream turbulent wakes. The computations were performed with 2.5 and 5.7×10^7 grid points on a parallel computer.

1. Introduction

Flow in turbomachinery has long been a source of interesting fluid dynamics. Distortion of the rotational part of the mean flow is integral to analyses of flow through turbine passages (Hawthorne & Novak 1969; McCune & Hawthorne 1976). However, the nature of the unsteady flow caused by rotor wakes passing through a stator passage is only now in the process of being understood (Sharma & Stetson 1998). In this paper we report an intriguing behaviour of those wakes.

The data presented herein are from a direct numerical simulation (DNS) of turbulent wakes swept past the inlet of a low-pressure turbine (LPT) cascade. The LPT is installed in jet engines upstream of the propelling nozzle, supplying power to the fan and first compressor stages. A feature of the LPT is that representative Reynolds numbers are in a range where DNS is practicable (Hodson 1998); also, the aspect ratio is relatively high and the Mach number relatively low. The present simulations are for a section of mid-span, with the incident mean wake vorticity parallel to the leading edge (figure 1). The flow is turned by more than 100° and accelerated by a factor of about 1.9, producing significant streamwise straining. The magnitude and direction of the principle axes of strain vary with position. These particular features – large rate of strain, varying orientation, incident wake – produce an intriguing vortical structure inside the turbine passage, which has not previously been discovered.

In our initial simulations, near-wall velocity signals revealed characteristics reminiscent of intense streamwise vortices on the concave, pressure side of the blade. The possibility of Görtler instability was raised. Görtler vortices are known to be determined by upstream conditions and to grow slowly (Floryan 1991). It seemed

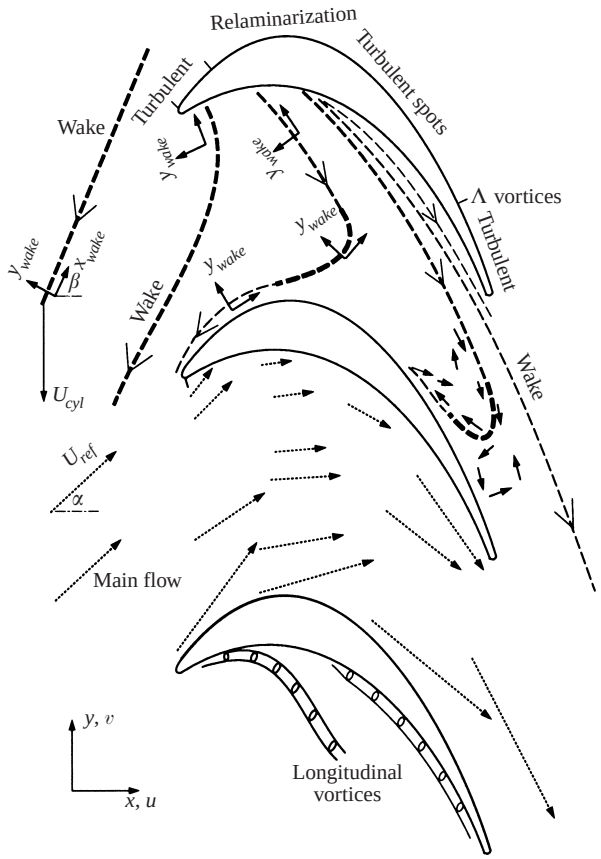

FIGURE 1. Sketch of the observed wake disotrtion, wake-induced transition, primary type longitudinal vortices as well as flow velocity vectors in the present simulation.

that other processes must be involved. The possibility also existed that large straining along the pressure surface was the primary source of the vortices; or were they simply highly strained Görtler vortices? Vortex identification in three dimensions using the DNS database provided convincing evidence that a new mechanism was at work. Hairpin vortices were being produced well above the wall, within the incident wake. They were then stretched along the surface, producing an opposite signed vortex in consequence of the viscous boundary condition; this, not Görtler instability, was causing the intense streamwise vortices. The features of this phenomenon provide intriguing observational fluid dynamics.

Various aspects of the distortion of (wake) vorticity have been studied in the literature. Sutera, Maeder & Kestin (1963) proposed a mathematical model for a steady, plane stagnation flow into which perturbation vorticity is introduced. They demonstrated that vorticity amplification by stretching of vortex filaments in the stagnation-point flow was an important mechanism. The essence of the model is that vorticity of a scale larger than a certain neutral scale, and appropriately oriented, can be selectively amplified as it is convected towards the stagnation point. Such vorticity, present in the oncoming flow with small intensity, can be greatly magnified in intensity and induce a large three-dimensional effect.

Sadeh (1968) injected smoke near a stagnation-point boundary layer and photographed the resulting flow pattern. Visualization showed that streamlines were wrapped around vortex cores in helical spirals, whose axis was in the streamwise direction.

Kestin & Wood (1970) attempted to mathematically explain Sadeh's visualization as an instability. They argued that a uniform flow approaching a two-dimensional stagnation point is inherently unstable; random disturbances carried by the free stream cause the flow to become three-dimensional. An analogy was drawn between this and concave boundary layer instability. However, to close their own analysis they resorted back to the vorticity amplification theory of Sutera *et al.* (1963).

The works of Lin & Corcos (1984) and Neu (1984) are of some tangential relevance. They studied the dynamics of a layer of vortices aligned parallel to the principal axis of a uniform plane straining flow. They found that an array of alternating vortices of elliptical cross-section with weak circulation will undergo slow decay due to viscous diffusion; but a layer of sufficiently strong vortices will buckle and break into a set of concentrated circular vortices. The process observed herein is somewhat different. No streamwise vortex sheet precedes the disruption of the wake into distinct vortices. It is unclear whether the analysis of roll-up of streamwise vortex sheets has a bearing on the problem of wake distortion.

DNS studies of idealized, strained turbulent wakes by Rogers (2000) suggest that the structure of the turbulence depends strongly on the orientation of the strain relative to the wake. Rogers (2000) visualized strained, temporally developing wakes using contours of spanwise vorticity magnitude over an (x, y)-plane. When *spanwise stretching* was applied, structures become more organized. Fewer vortical eddies were seen across the streamwise direction, and regions of apparently non-vortical fluid emerged. As time progressed, the stretched vortical structures tended to amalgamate with other vortical regions of the same sign, further increasing the apparent organization of the flow.

Wakes under *spanwise compression* exhibited many small-scale vortical eddies with little over-all large-scale coherence or organization. Rogers felt his results were consistent with previous experiments of Keffer (1965), and with the analysis of Lin & Corcos (1984).

Our flow is perhaps more analogous to the simulations of *streamwise* straining. Rogers found that with streamwise stretching (his Case D), there were significant non-vortical regions and the vortical eddies were quite elongated along the x-axis of the wake. Streamwise compression (Case C) brought about many small-scale structures and rapid growth of wake width. Large-scale organized motions were not able to develop in the presence of streamwise compression and cross-stream stretching. These observations are suggestive of the strained migrating wake behaviour seen near the pressure and suction sides of the turbine passage.

2. Numerical considerations

2.1. *Problem definition*

Consider the evolution of an incompressible flow through a smooth turbine passage, as in figure 1 and figure 2. Upstream wakes traverse the inlet periodically. The Cartesian system x-, y- and z-axes refer to the axial, tangential and spanwise directions, respectively. Lengths are normalized by the blade axial chord L. The blade pitch is 0.9306, and true chord length is 1.1647. Inlet and outlet planes of the computational

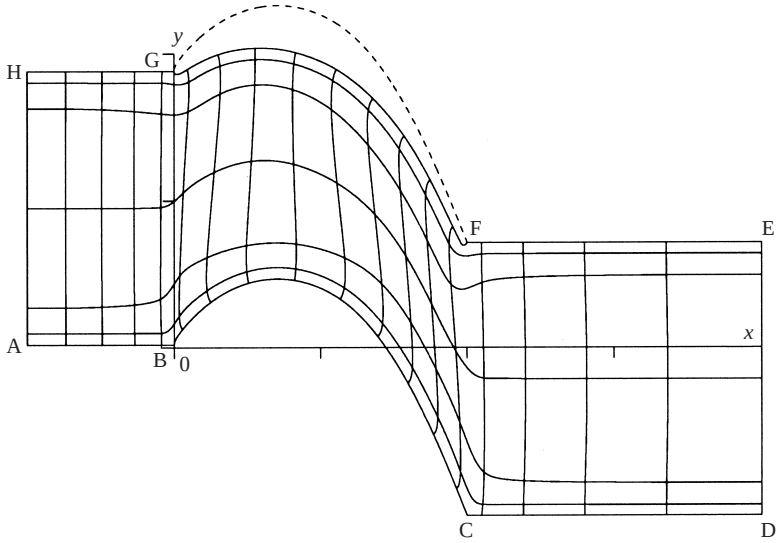

FIGURE 2. Cross-sectional view of the computational domain and one level of multigrid mesh (1153/64, 385/64, 129/129); B (0.0, 0.010289), C (1.0, −0.572873), F (1.0, 0.357727), G (0.0, 0.940887).

domain are at $x = -0.5$, and $x = 2.0$, respectively. The spanwise dimension is prescribed as 0.15. That was found to be sufficient for independence of the computations from the size of the computational domain.

Upstream, the flow velocity is $U_{ref} = 1.0$, and makes an angle $\alpha = 37.7^\circ$ with the x-axis. The characteristic Reynolds number is then $Re = U_{ref}L/\nu$ where ν is the kinematic viscosity of the fluid. Throughout this study $Re = 1.48 \times 10^5$. The designed exit flow makes an angle of -63.2° with the x-axis.

The wakes are generated by imaginary circular cylinders moving in the y-direction at $U_{cyl} = -1.2048$. The cylinders are equally spaced so that they cut through an (x, z)-plane at a specified passing period $\mathscr{T}$. For the given pitch and U_{cyl}, $\mathscr{T} = 0.7724$. The mean flow properties of the wake correspond to those produced by 0.01177 diameter cylinders positioned at $x = -0.33$.

The blade, named T106, has been used for a number of compressible flow measurements reported by Weiss & Fottner (1995), Engber & Fottner (1996) and Duden, Raab & Fottner (1999). Most of that work was on secondary flow and endwall effects. The blade profile is representative of those in LPTs.

2.2. *Governing equations and notation*

Mass and momentum conservation are enforced by solving the full time-dependent, continuity and Navier–Stokes equations:

$$\nabla \cdot \boldsymbol{u} = 0, \tag{2.1}$$

$$\frac{\partial \boldsymbol{u}}{\partial t} + \nabla \cdot (\boldsymbol{u}\boldsymbol{u}) = -\frac{1}{\rho}\nabla p + \nabla \cdot \left\{ \frac{1}{Re}[\nabla \boldsymbol{u} + (\nabla \boldsymbol{u})^s] \right\}, \tag{2.2}$$

where $\boldsymbol{u}$ is the velocity vector and superscript $\mathscr{S}$ denotes transpose. The equations are in non-dimensional form.

In this paper, time-averaging is represented by an overbar. Averaging at a particular phase, $t^m_{n_\mathscr{T}} = m\mathscr{T} + n_\mathscr{T}\mathscr{T}$, is denoted by $\langle\cdot\rangle$, where m is any integer. $0 \leqslant n_\mathscr{T} \leqslant 1$ is the

fraction of the wake passing period. For example, the phase-averaged mean velocity components are evaluated as

$$\langle u_i \rangle(t_{n_{\mathscr{T}}}) = \frac{1}{M} \sum_{m=1}^{M} u_i(t^m_{n_{\mathscr{T}}}), \tag{2.3}$$

where M is the total number of periods within which phase-averaging is performed. Additional averaging over the spanwise, z, direction is implied in both time-averaging and phase-averaging. Time-averaged and phase-averaged mean velocities are related via $\bar{u}_i = \overline{\langle u_i \rangle}$. Thus the instantaneous velocity can be decomposed as

$$u_i = \langle u_i \rangle(t_{n_{\mathscr{T}}}) + u'_i(t_{n_{\mathscr{T}}}) = \bar{u}_i + \tilde{u}_i(t_{n_{\mathscr{T}}}) + u'_i(t_{n_{\mathscr{T}}}), \tag{2.4}$$

where $\tilde{u}_i(t_{n_{\mathscr{T}}}) = \langle u_i \rangle(t_{n_{\mathscr{T}}}) - \bar{u}_i$ is the periodic velocity fluctuation with respect to the time-averaged mean, and $u'_i(t_{n_{\mathscr{T}}})$ is the true stochastic turbulence fluctuation.

2.3. *Grid generation*

DNS poses a more stringent mesh requirement than Reynolds-averaged computation. For the present case, turbulence carried by the wake needs to be resolved in the upstream flow, in the free stream inside the turbine passage, and on the blade wall boundary layers. These requirements favour use of an H-type mesh. Unfortunately, even with the use of an elliptic grid generation scheme, the high degree of distortion of the computational domain shown in figure 2 results in discontinuity of the grid transformation Jacobian in the interior, since the control functions evaluated at the boundaries (near $x = 0$ and $x = 1$) are not smooth. We have been able to generate an H-type grid with good quality in the turbine passage by applying parabolic smoothing to the control functions appearing in the elliptic grid generation scheme of Hsu & Lee (1991). The mesh possesses continuous derivatives to the second order in the interior of the computational domain (e.g. $\partial^2 x/\partial \xi^2$, ξ is the streamwise curvilinear coordinate) and the grid lines are nearly orthogonal to boundaries (figure 2).

2.4. *Inflow, cyclic and other boundary conditions*

Inflow boundary conditions, including the manner by which wakes are introduced into the computational domain, are nearly identical to those documented in Wu *et al.* (1999) and Wu & Durbin (2000*a*, *b*). In the present computation, equation (7) of Wu *et al.* (1999) takes the following modified form:

$$\left.\begin{aligned} u_{inflow} &= u_{ref} \cos\alpha + \left(\cos\beta \sum_{q=1}^{\mathscr{N}} u_{eff,wake,q} - \sin\beta \sum_{q=1}^{\mathscr{N}} v_{eff,wake,q} \right), \\ u_{inflow} &= u_{ref} \sin\alpha + \left(\sin\beta \sum_{q=1}^{\mathscr{N}} u_{eff,wake,q} - \cos\beta \sum_{q=1}^{\mathscr{N}} v_{eff,wake,q} \right), \\ w_{inflow} &= \sum_{q=1}^{\mathscr{N}} w_{eff,wake,q}, \end{aligned}\right\} \tag{2.5}$$

where α and β are defined in figure 1, and all other notation conforms to that in Wu *et al.* (1999). For the flow conditions described in § 2.1, the inlet maximum wake deficit and wake half-width are prescribed as 0.18 and 0.04, respectively; u_{eff} is obtained from a separate simulation of an evolving wake. The fully developed wake is swept across the inflow boundary. The transformation (2.5) is from the 'rotor' frame of the wake generator, to the 'stator' frame of the passage.

Compared to flows around an isolated airfoil, the most distinctive geometric feature of turbomachinery flows is its repetitiveness in the tangential, y-direction. In a typical axial turbine passage the pitch-to-chord ratio is about 1. This distance is substantially larger than the length scales of the turbulent eddies inside the blade boundary layer, and also larger than those contained in the incident wake. For these reasons, little error is caused when the two boundary pairs AB/HG, and CD/FE (figure 2) are treated as both statistically and instantaneously periodic; this is an artifice of using a single passage.

With the choice of a H-grid, the upper (HE) and lower (AD) boundaries are of hybrid type: part cyclic and part no-slip. This poses potential problems for solution of the discretized Poisson equation: although arguments exist that no boundary condition for the discretized Poisson equation is necessary, in practice homogeneous Neumann conditions are applied on all non-cyclic boundaries (Rosenfeld & Kwak 1993; Wu *et al.* 1999). In the present work, a homogeneous Neumann condition for pressure is applied on inflow and outflow boundaries, AH/DE, as well as on turbine blade surfaces BC/GF. On the pairs AB/HG and CD/FE cyclic matching is applied to the pressure and the associated velocity.

2.5. *Computational details*

Numerical integration is by the fractional step method of Rosenfeld, Kwak & Vinokur (1991) for unsteady, incompressible Navier–Stokes equations in generalized coordinate systems. The governing equations are discretized by finite volumes on a staggered mesh. The dependent variables are pressure p and volume fluxes across the faces of the cells. Transformation between Cartesian velocity components and volume fluxes is made using area vectors and their reciprocals (Rosenfeld *et al.* 1991). Divergence-free flow is obtained by solving a discrete Poisson equation (Rosenfeld & Kwak 1993).

Convergence of the discretized Poisson equation was accelerated by the multigrid method, after Fourier transformation along the span. For each wavenumber, the decoupled two-dimensional Helmholtz system is solved using a V-cycle multigrid subroutine. Following Rosenfeld & Kwak (1993), cell-wise coarsening is adopted instead of the usual pointwise coarsening. Scalable parallelization is achieved with the OpenMP Fortran Application Program Interface.

Simulations were performed on a 57 million point grid (1153, 385, 129 points in the streamwise, wall-normal and spanwise directions, respectively) and a preliminary simulation was done on a 25 million point grid (769, 257, 129). In the fine grid, 288 streamwise points are distributed upstream of the leading edge along AB/GH, and 576 points are used on the blade along BC/FG. The grid used in Wu *et al.* (1999) on a flat plate was (1025, 401, 129). The Reynolds number and characteristic computational domain dimensions are similar for the present flow and that in Wu *et al.* (1999). Hence, we have relied on extensive resolution studies in that simpler geometry.

The theme of this paper does not demand extensive discussion of grid resolution, but some comments are in order. Figure 2 shows a subset of the fine computational grid (1153, 385, 128). Along the streamwise and normal directions, only one out of 64 grid points is plotted. Subsequent contour plots are produced using the full grid, but the vector plots (figures 4*b*, 11, etc.) were drawn using a subset of the full computational grid. In addition, all the three-dimensional contour surface plots (e.g. figure 14) were also drawn using a subset of the full grid so that post-processing could be done within the computer memory limit. Near the suction-side trailing edge, where the boundary layer is transitional, there are approximately 35 to 40 points

inside the boundary layer, in the transverse direction. Note there is a total of 385 points in this direction: the majority of points are distributed in the turbine passage, which serves the purpose of this investigation, since our primary concern is to resolve the distorted wake. Other investigations on boundary layer dynamics most likely would adopt a reverse strategy, using fewer points for the wake inside the passage. For the coarse resolution test (769, 257, 129) we used a more severe stretching factor along the y-direction to compress the grids towards the wall. Figure 3 compares the wall-static pressure coefficient using the two sets of grids. It is not illustrated here, but the coarse grid shows the same wake distortion scenario as will be presented below. The phenomena of interest were found to be insensitive to grid resolution.

In the multigrid procedure for the Poisson solver, the computational mesh is halved six times. A maximum of three V-cycles is applied at each time step, and three pre- and post-successive line over-relaxation iterations are applied for every cycle. The residual threshold was set to 10^{-7}.

The time step was $\mathrm{d}t = 1.295 \times 10^{-4}\mathscr{T} = 1.0 \times 10^{-4} L/U_{ref}$. This maintains a CFL number less than 1. Such a criterion is mandated by requirements of stability and time accuracy. It has been found satisfactory in many DNS studies, and certainly suffices for the present study of wake distortion. The velocity field was allowed to evolve for about 5 wake passing periods (38 620 dt) and statistics were then collected for another 10 wake passing periods. Phase-averaging was performed by dividing each passing period into 25 equal subdivisions. The computation was carried out on an SGI Origin 2000s using 64 processors.

3. Distorted migrating wakes and straining

In this section we describe the distortion of migrating wakes in the turbine passage by the base-flow strain rate field. The material will facilitate subsequent discussion on the main subject of the paper: longitudinal vortices evolved from strained wakes.

Figure 3 shows the wall static-pressure coefficient $C_{pw} = 2(\bar{p} - \bar{p}_A)/U_{ref}^2$. Experimental data are from measurements on the T106 blade, kindly made available to us by Dr Peter Stadtmueller of the Universität der Bundeswehr München in Germany. Small discrepancies between the simulation and experiments might be attributed to endwall effects, different inflow conditions and compressibility. In the experiments the inflow was seeded with grid turbulence but with no passing wakes. The span-to-chord aspect ratio was only 3 – which, still, is relatively large compared to high-pressure turbines.

The focus of the present paper is on vortices near the pressure side of the passage. Flow near the pressure surface is under zero pressure gradient from $x_w = 0.015$ to 0.6, after which it changes to sharply favourable. Subscript w refers to a surface value. On the suction surface, favourable streamwise pressure gradient dominates from $x_w = 0.03$ to 0.6, followed by a strong adverse pressure gradient. In a short region on the suction side near the leading edge ($x_w < 0.03$) there is a very strong adverse pressure gradient.

Principal stresses σ_1 (positive) and σ_2 (negative) of the mean strain rate tensor S_{ij} are plotted in figure 4(*a*). Arrows indicate directions of the principal axes. Inside the turbine passage, except near the suction-side leading edge, σ_1 is directed approximately towards the turbine exit flow direction, and σ_2 is directed roughly in the turbine inflow direction. A fluid element is stretched in the direction of σ_1 and compressed along the direction of σ_2.

The magnitude of the strain rate is stronger near the suction side of the blade. Because the migrating wake changes its orientation inside the passage (figure 1), the

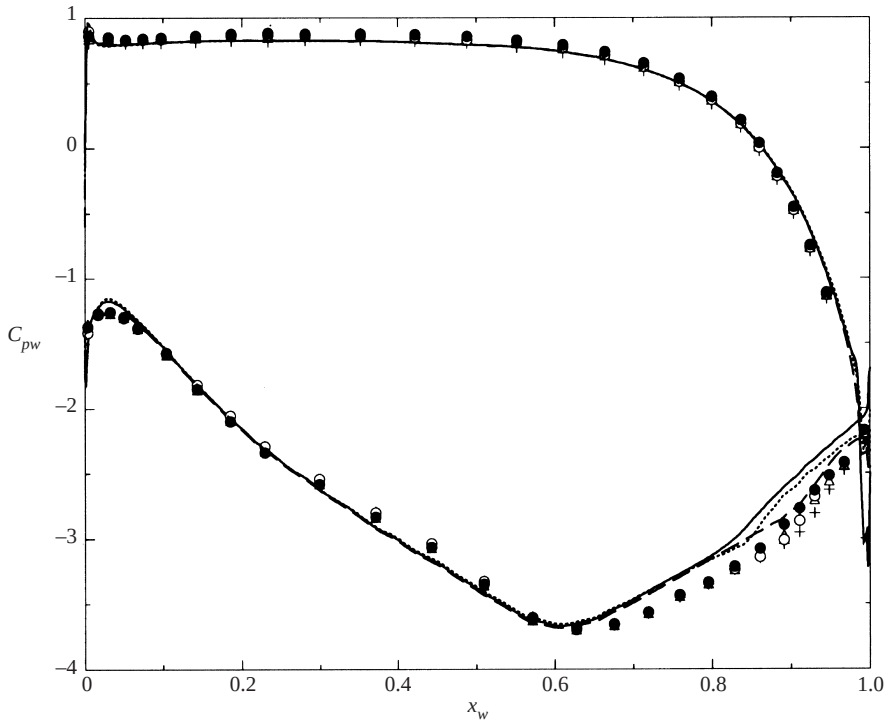

FIGURE 3. Time-averaged wall static-pressure coefficient C_{pw}; present DNS: ——, (no wake); ——, (with wake, 769 × 257 × 129 mesh); ·····, (with wake, 1153 × 385 × 129 mesh). The symbols are experiments by Professor L. Fottner's group at Universität der Bundeswehr München with varying inlet free-stream turbulence intensity and Mach number, but without an upstream passing wake.

directions of σ_1 and σ_2 intersect the wake axes differently near the pressure side from near the suction side. This is illustrated in figure 4(*b*). Near the pressure side, compression is applied along y_{wake} and stretching is applied along x_{wake} (figure 1). At the bow apex, where the wake is bent backwards near the suction side, stretching is applied along y_{wake} and compression is now in the x_{wake} direction. In figure 4(*b*) the bold double arrows indicate fluid velocity relative to a material element centred in the local wake reference frame. The type of strained wakes sketched near the pressure-side surface corresponds roughly to Case D of the temporally developing strained wake simulations by Rogers (2000); the type of strained wakes sketched at the bow apex side corresponds to his Case C. Rogers found velocity deficit, width and turbulence fluctuations in Case C to increase with time; they all decayed in the Case D wake. The explanation is quite simple: a temporally developing parallel flow consisting of a mean rate of strain plus a wake is $U = ax + U_{wake}(y,t)$, $V = -ay$. If the wake defect is defined by $\Delta = \int_{-\infty}^{\infty}(U_\infty - U_{wake}(y))\mathrm{d}y$, then the x-momentum equation shows that $\mathrm{d}\Delta/\mathrm{d}t = -2a\Delta$ (Rogers 2000). If the straining is positive along the wake, $a > 0$ and the defect will be weakened; if it is negative the defect increases.

A pair of spanwise, counter-rotating vortices separated by the thickening bow apex

FIGURE 4. (*a*) Principal stresses and principal axes σ_1 (dark arrows) and σ_2 (light arrows) of the mean strain rate tensor S_{ij} (without wake) inside the turbine passage; ——, $\sigma_1 = 1.25$; ——, $\sigma_1 = 1.75$; ·····, $\sigma_1 = 2.25$; —·—, $\sigma_1 = 2.75$; – – –, $\sigma_1 = 3.25$. (*b*) Periodic fluctuating velocity vectors of the wake passing flow at one phase; × mark $0.1 \leqslant x_w \leqslant 0.9$ with increment 0.1.

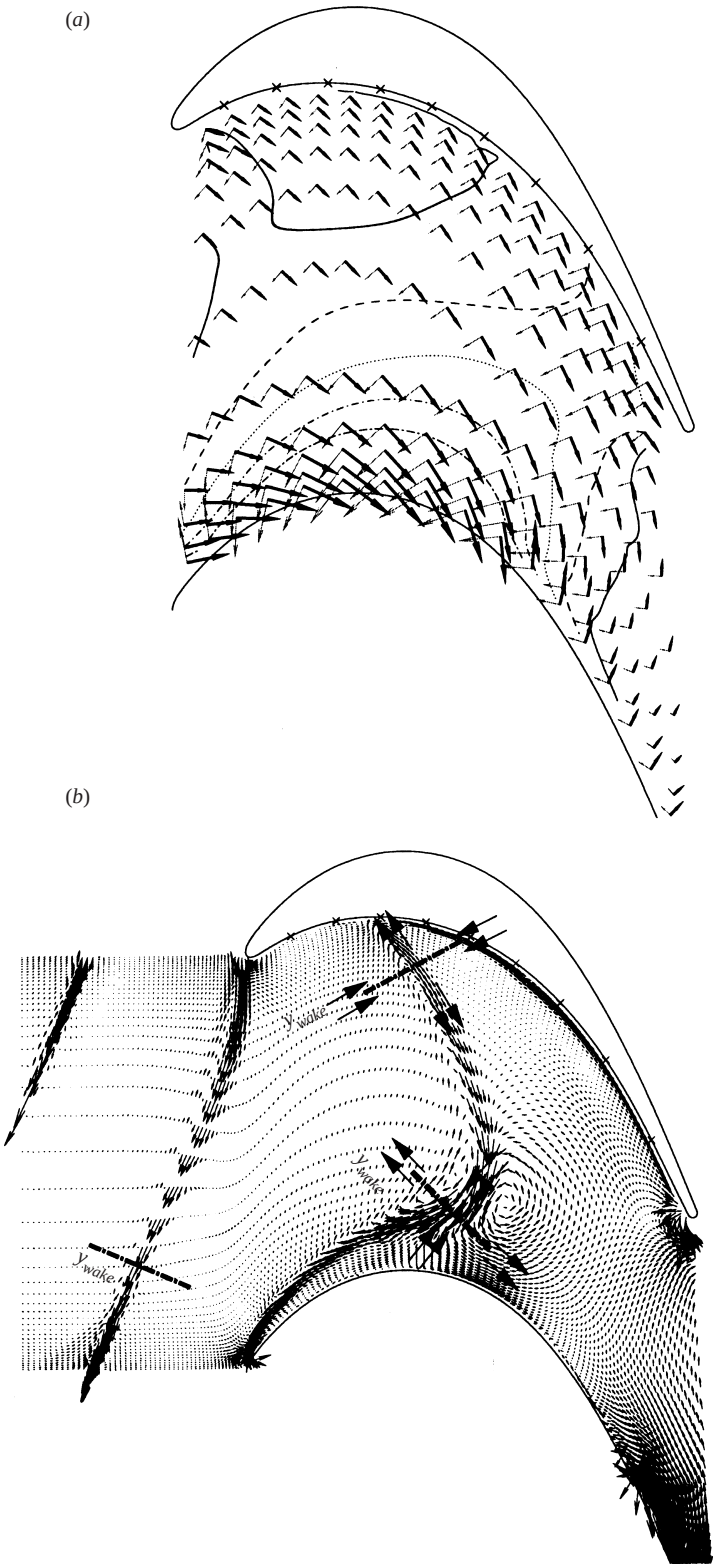

FIGURE 4. For caption see facing page.

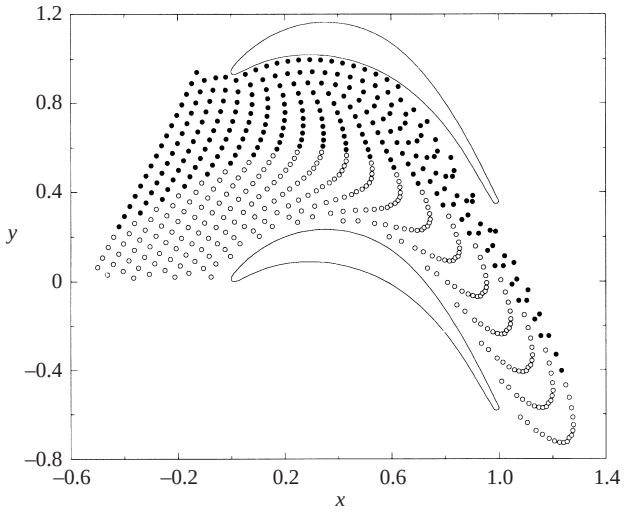

FIGURE 5. Integrated effect of the mean strain rate tensor S_{ij} on passive particles having the same inlet inclination angle as the upstream wake.

is apparent in figure 4(*b*). This can be explained as a local concentration of vorticity produced by convection. Consider the motion of a streak of passive material particles through the turbine passage in the given base-flow velocity field. Figure 5 illustrates their motion. The particles are released into the time-averaged mean velocity field at the same inclination angle β as the inlet wake. Solid and open circles in the figure help to visually identify a particular material particle. Connecting the trajectory of a marked particle makes a pathline. The apparent similarity between the distorted passive material streak in figure 5 and the distorted migrating wakes in figure 1 and figure 4(*b*) demonstrates that convection and straining by the irrotational base-flow velocity field dominate the wake deformation process.

Figure 4(*b*) shows that after being segmented at the leading edge, the suction-side and pressure-side wakes behave differently. The suction-side portion wraps around the stagnation point and is pulled toward the surface by the flow. The pressure-side portion is under the action of a velocity field with nearly uniform direction but increasing strength away from the wall (figure 1). The direction of the convective velocity is nearly perpendicular to the wake axis x_{wake}. The wake is thus rotated slowly in the counter clockwise direction and convected downstream. Elongation of the wake is gradual and is nearly transverse to the base flow. Along the downstream half of the pressure surface, the flow velocity undergoes a change in direction and increase in magnitude. The velocity is turned such that it becomes nearly parallel to the wake axis x_{wake}. The resulting strong streamwise velocity gradient severely strains the wake, dramatically stretching and thinning it.

Figure 6 shows contours of instantaneous velocity magnitude over one (x, y)-plane at three consecutive instants within one wake passing period. These cross-sectional plots give the locations of the migrating wake at selected phases, and can be used as references in subsequent discussion.

Prior to entering the passage, the wake defect flows against the inflow – towards negative y and negative x. Once a bow is formed, contours inside the upper arm bulge towards positive y and negative x. This is due to the turning of the base flow. The velocity deficit in the original wake is converted to an excess. The excess diminishes

as the wake is shifted towards the downstream half of the pressure surface. Stretching of wake material particles parallel to the wall (figure 5) reduces the density of mean spanwise vorticity, weakening the flow.

Relatively strong turbulent fluctuations at the bow apex after the summit are seen in figure 6. These fluctuations originate well away from the wall. This is a result of the vorticity concentration from the streamtube convergence shown in figure 5. Vortex stretching in the streamwise direction after the summit further enhances turbulence in the apex region. Alternatively, the Reynolds stress transport equation shows that the strain production term for $\overline{u'^2}_{wake}$ is positive when compression is along the x_{wake}-axis, as at the apex. The intensification of wake turbulence at the apex and decay near the pressure surface are qualitatively consistent with the results from Case C and Case D in Rogers (2000), respectively.

Figure 7 contains contours of instantaneous velocity magnitude in one (x, y)-plane for the flow without inlet wakes. Counter-rotating spanwise cells can be inferred near the suction surface trailing edge. These are caused by inflectional instability under the adverse pressure gradient. The base-flow, no wake, simulation was initiated with a restart file from the simulation with inlet wakes. In the absence of inlet wakes, the flow returns to laminar as the simulation progresses, except near the trailing edge where an instability is maintained.

4. Transition on the suction side

When wakes are present, transition occurs near the leading edge, but the flow quickly relaminarizes on the suction surface. The tangential velocity component immediately adjacent to the blade is shown at three consecutive instants in figure 8. The front of the blade remains turbulent at all times because of the strong local adverse pressure gradient (figure 3) and because of the way the wake wraps around the leading edge, producing a persistent disturbance. Toward the back of the blade, after $x_w = 0.6$, an adverse streamwise pressure gradient again prevails. Transition is mediated by turbulent spots (Wu *et al.* 1999), which are seen to form near mid-chord, to grow, and to merge into the trailing-edge, fully turbulent region. This is a bypass transition process.

Figure 9 shows that the base-flow is laminar except very close to the trailing edge. There the suction-side adverse pressure gradient generates an inflection point instability, producing spanwise rolling cells and instantaneous back flow. This is in turn followed by Λ vortices, and transition. In other words, the transition in the absence of wakes is reminiscent of orderly transition (Kleiser & Zang 1991). When inlet wakes are present bypass mechanisms dominate (Wu *et al.* 1999).

Contours in figure 8 on the pressure-side surface display large-amplitude spikes. They move slowly with time and are most apparent for $x_w \geqslant 0.5$ where strong streamwise stretching occurs. They are symptomatic of an intriguing phenomenon.

Figure 10 plots instantaneous fluctuating velocity vectors immediately adjacent to the pressure side of the blade. The fluctuating velocity is defined relative to the spanwise-averaged mean flow. Vectors pointing towards the upstream direction form long narrow axes, corresponding to the low-momentum fluid suggested by the spikes in figure 9. In figure 10, the precursor of the narrow axes seem to be the relatively large spanwise features in the region of $0.1 \leqslant x_w \leqslant 0.2$. Views like this raised the question of whether Görtler vortices were being triggered by concave curvature. Although the surface is indeed curved, disturbances are also subjected to intense stretching toward the rear of the suction surface (figure 5); the features may not be a signature of

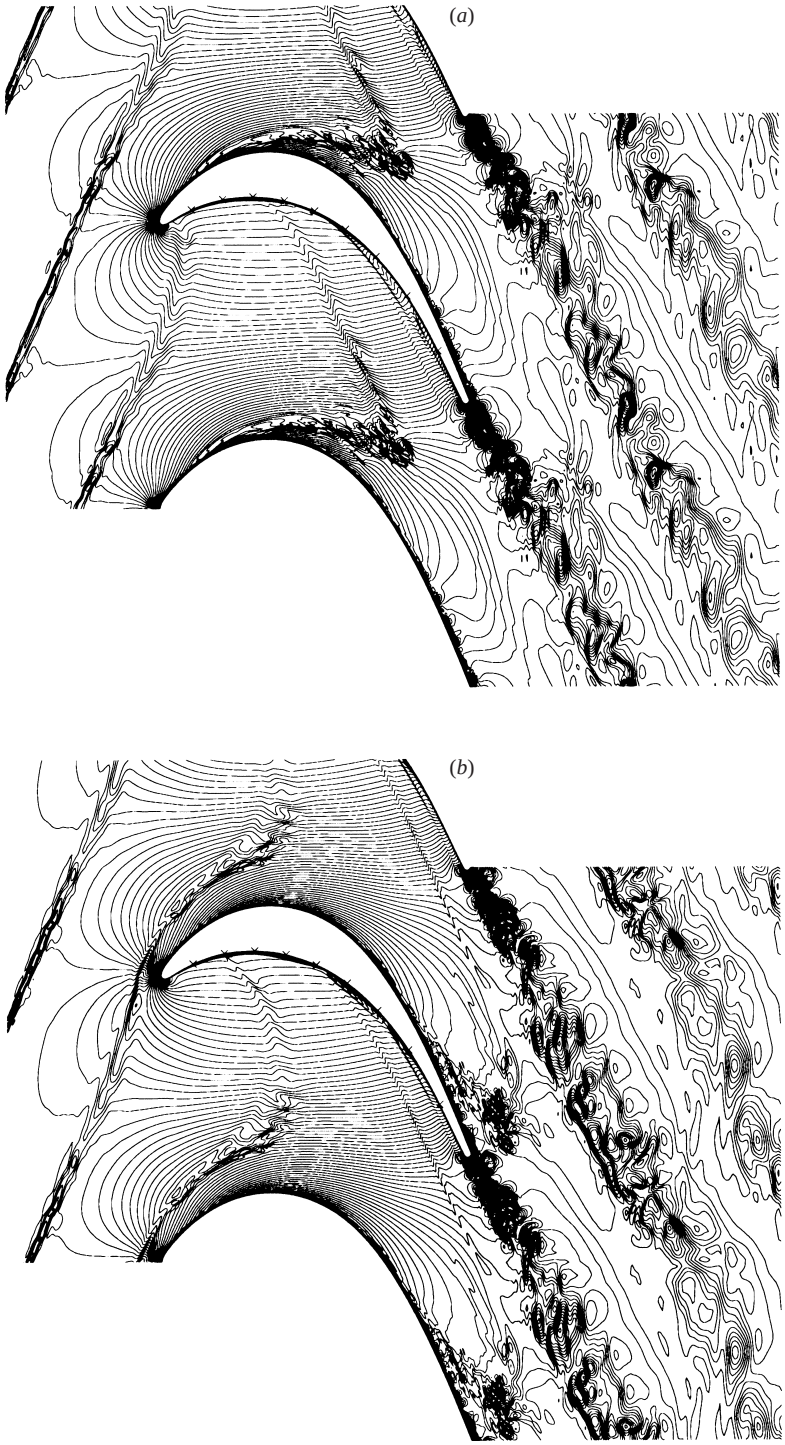

FIGURE 6 (*a*, *b*). For caption see facing page.

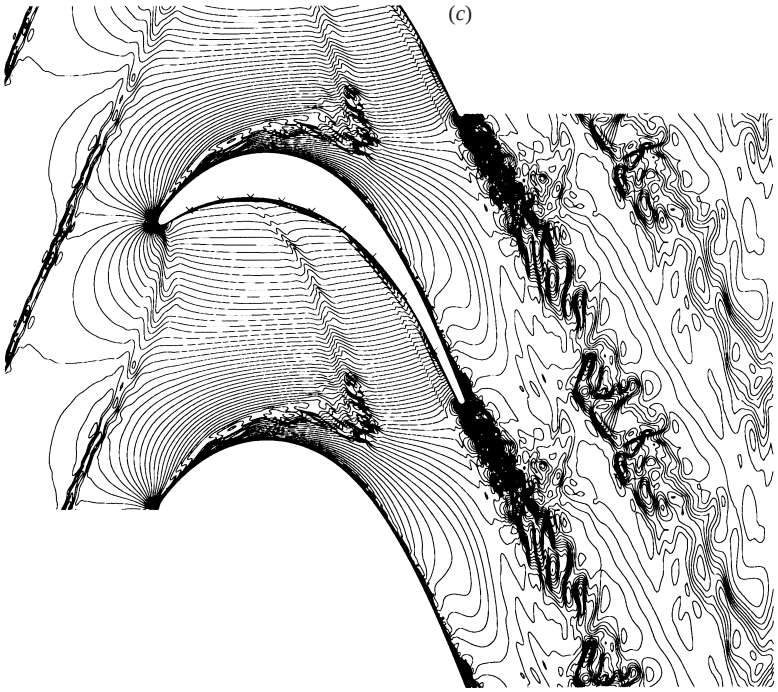

FIGURE 6. Velocity norm over the (x, y)-plane, $z = 0.0$; $\times$ marks $0.1 \leqslant x_w \leqslant 0.9$ with increment 0.1. (*a*) $t = 7.61\mathscr{T}$, (*b*) $8.19\mathscr{T}$, (*c*) $8.52\mathscr{T}$.

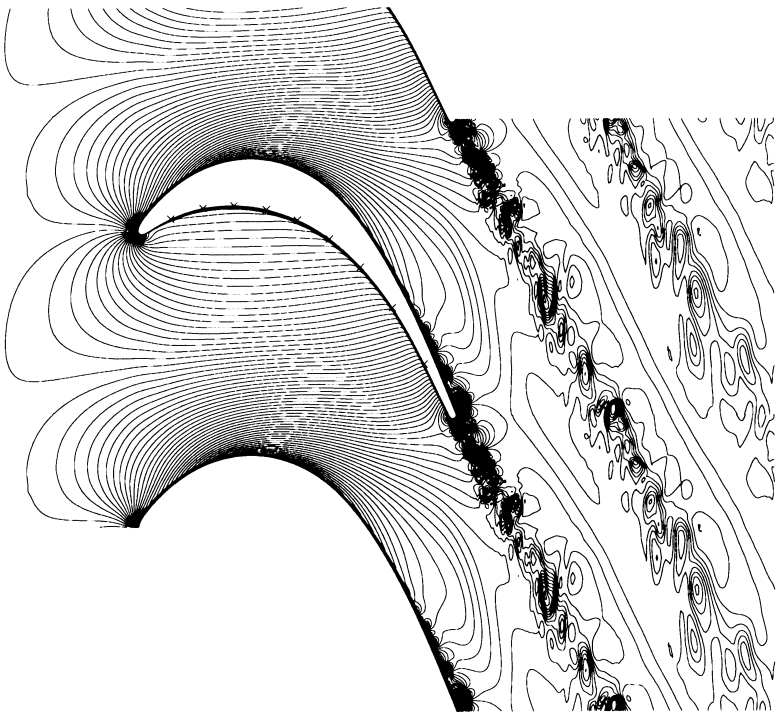

FIGURE 7. No wake: velocity norm over the (x, y)-plane, $z = 0.0$ at one instant; $\times$ marks $0.1 \leqslant x_w \leqslant 0.9$ with increment 0.1.

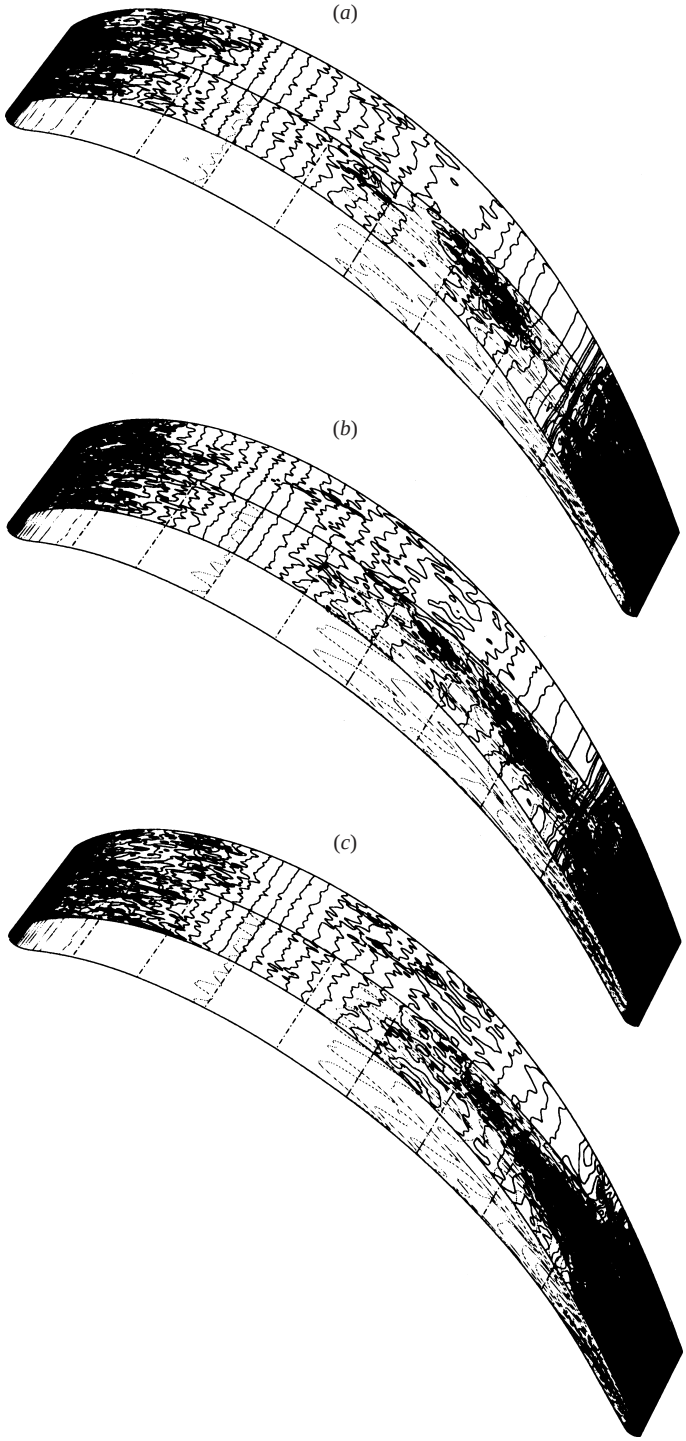

FIGURE 8. v velocity component over the suction (dark lines) and pressure (light lines) surfaces at three instants; $-\cdot-$ marks $0.1 \leqslant x_w \leqslant 0.9$ with increment 0.1. (*a*) $t = 7.73\mathscr{T}$, (*b*) $7.86\mathscr{T}$, (*c*) $8.00\mathscr{T}$.

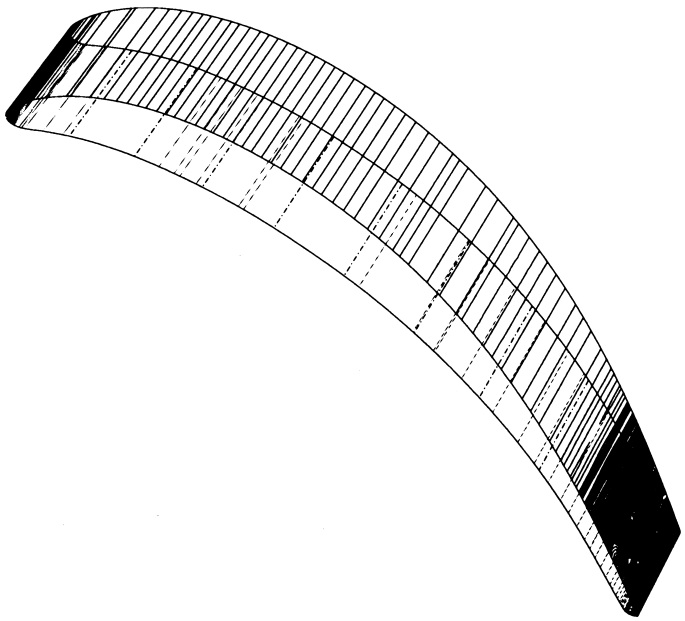

FIGURE 9. No wake: v velocity component over the suction (dark lines) and pressure (light lines) surfaces at one instant; $-\cdot-$ marks $0.1 \leqslant x_w \leqslant 0.9$ with increment 0.1.

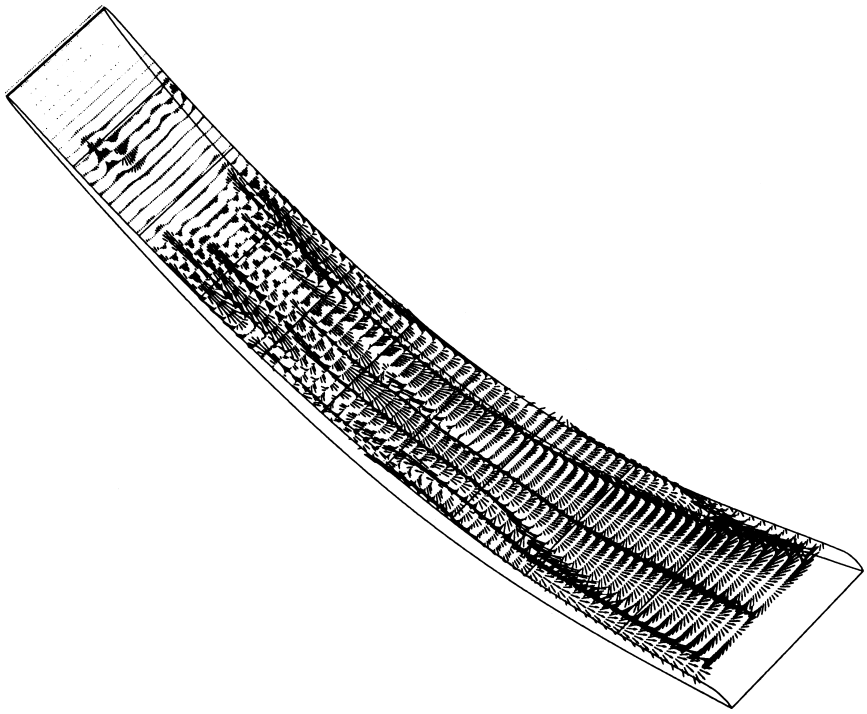

FIGURE 10. Instantaneous fluctuating velocity vectors (with respect to spanwise-averaged mean) adjacent to the pressure surface at $8.00\mathscr{T}$; —— marks $0.1 \leqslant x_w \leqslant 0.9$ with increment 0.1.

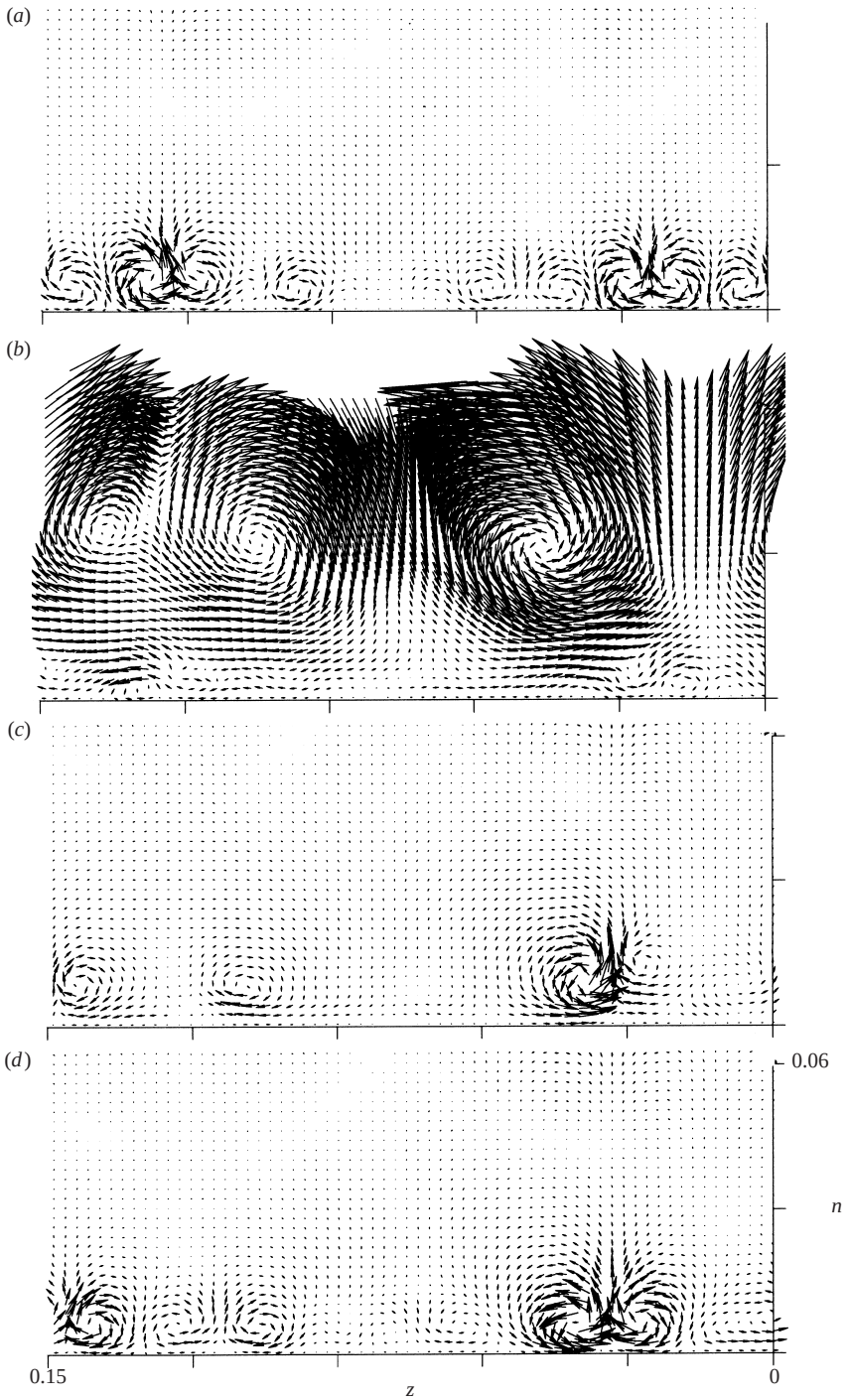

FIGURE 11 (*a–d*). For caption see facing page.

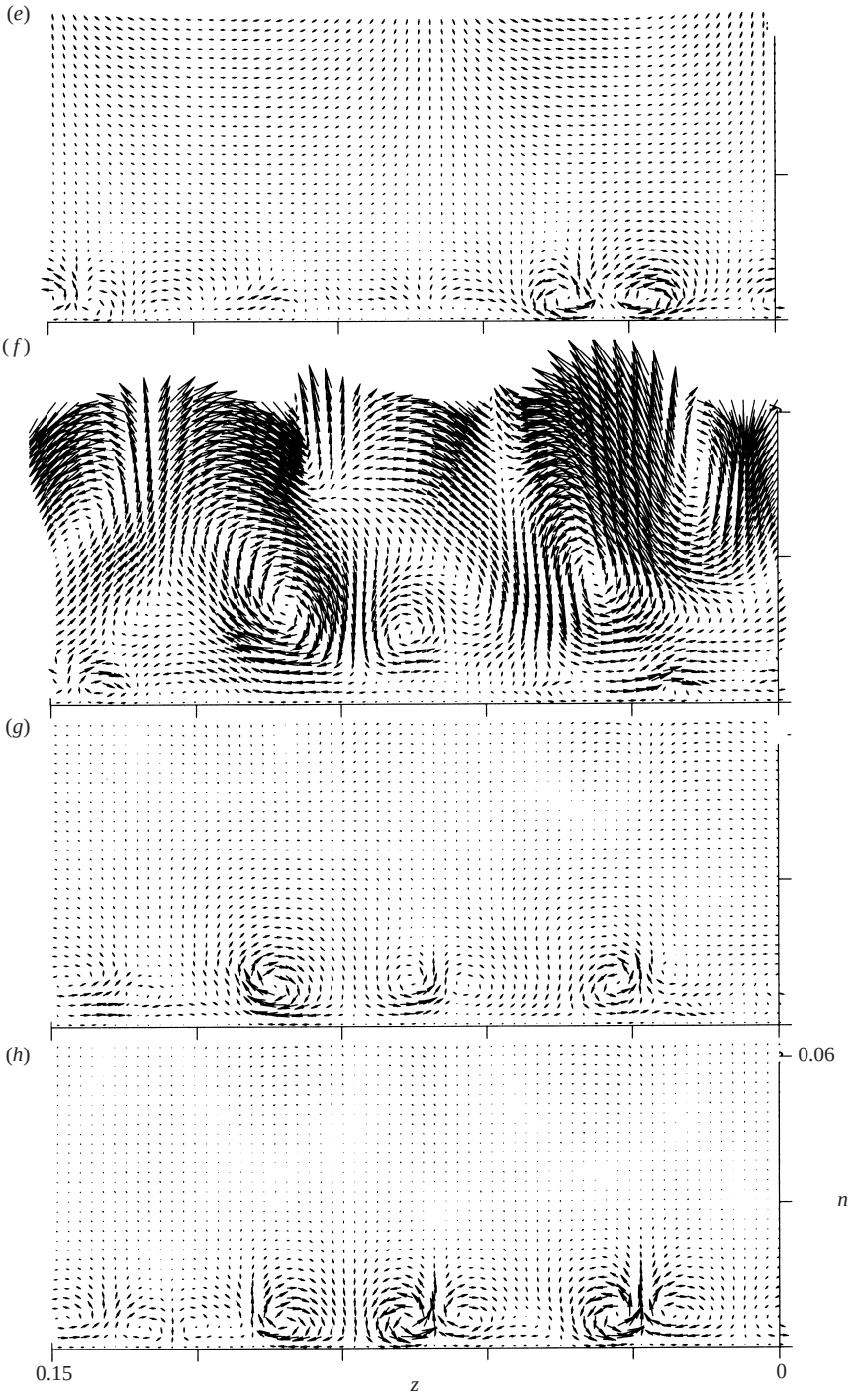

FIGURE 11. Fluctuating velocity vectors (spanwise-averaged mean subtracted) in the plane perpendicular to the pressure surface at $x_w = 0.3$. (*a*) $t = 8.00\mathscr{T}$, (*b*) $8.38\mathscr{T}$, (*c*) $8.63\mathscr{T}$, (*d*) $t = 8.96\mathscr{T}$, (*e*) $9.22\mathscr{T}$, (*f*) $9.43\mathscr{T}$, (*g*) $9.59\mathscr{T}$, (*h*) $10.00\mathscr{T}$.

Görtler vortices. The origin of these near-surface streaks was investigated by various vortex identification methods, as described in the following sections.

5. Vortices identified in spanwise and wall-normal planes

Velocity vectors in planes normal to the surface show clearly that the flow features are vortices, not jets, along the surface. Figure 11 shows fluctuating velocity vectors over a spanwise section at $x_w = 0.3$, covering 8 consecutive instants over 2 wake passing periods. The wall-normal distance extends from 0 at the pressure surface to 0.06 inside the passage. The spanwise-averaged mean has been removed from the vectors. The spatial locations of the free-stream passing wakes at different phases can be found by referring to figure 6. Vectors are shown only at a small subset of the computational nodes.

Counter-rotating vortex pairs with varying strength are seen in figure 11(*a*). Unequal strengths can be seen even between the two vortices within a single pair. We are interested in their connection with the free-stream passing wake.

The sequence of figures 11(*b*)–11(*f*) covers one full wake passing period, from $8.38\mathscr{T}$ to $9.43\mathscr{T}$. At both ends of the time interval, the migrating wake intersects this particular plane. The three strong, large rotating cells in figure 11(*b*) centred at $n \approx 0.03$ are from the passing wake. The origin of these fairly regular structures is discussed in § 6.

Figure 11(*c*) shows that after the free-stream wake has passed this cross-section plane, a disturbance lingers in the near-wall region. There are three isolated vortices near the wall, each having the same sense of rotation as its precursor – the cell higher above the wall but at approximately the same z at the earlier time, $t = 8.38\mathscr{T}$, of figure 11(*b*). It will be shown in § 6 that both cells belong to the same vortex element. The vortex at $0.03 < z < 0.06$ is stronger than the other two, so they sum to zero across the span, as required.

As the primary vortices descend towards the wall, they induce vortices with the opposite sense of rotation under the constraint of no-slip. Figure 11(*d*) shows how pairs of counter-rotating vortices are formed. Finally, figure 11(*e*) shows how the vortices attenuate as they begin to be overwhelmed by the next passing wake, arriving in figure 11(*f*). The process repeats beneath the new wake.

The streamwise velocity component is contour plotted in figure 12. Actually, only the contours of the negative fluctuating streamwise velocity are plotted for better visualization. The spanwise and wall-normal plane is now at $x_w = 0.7$. The times shown are the same as in figure 11. The wake passes this plane at a later time because it is farther downstream. The mushroom shape of these contours is typical of low-speed streaks produced by upwash of counter-rotating vortex pairs (Lee & Liu 1991). In between the vortices in a pair, low-momentum fluid is transported away from the wall, and is spread laterally as it flows up and over them. The stems of the mushrooms correspond to the narrow, negative fluctuating velocity axes shown in the vector plot of figure 10. For example, the five axes in figure 10 ($t = 8.00\mathscr{T}$) at $x_w = 0.7$ are the streamwise–spanwise cut through the five mushrooms appearing in figure 12(*a*).

In figure 12 the majority of the mushrooms are seen to be asymmetric: the larger half is associated with the stronger of the two counter-rotating vortices in one pair. Decay, merger and growth of the mushrooms can be observed in the figure. When a single strong vortex from the wake descends towards the surface, multiple mushrooms in the nearby region experience substantial modification and re-organization. Further

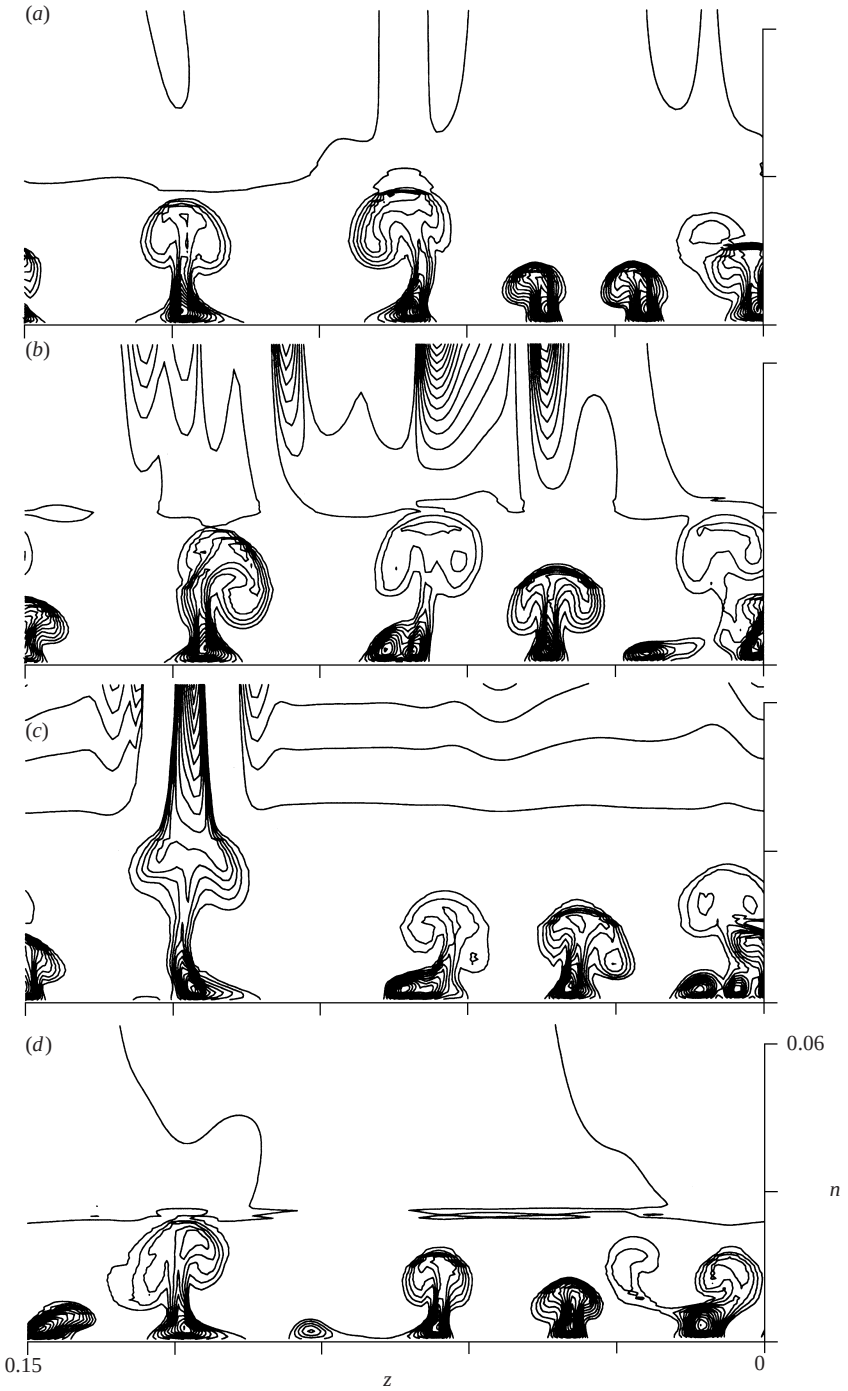

FIGURE 12. Negative fluctuating streamwise velocity component (with respect to spanwise-averaged mean) in the plane perpendicular to pressure surface at $x_w = 0.7$; contour level from 0 to -0.3 with increment -0.015. (*a*) $t = 8.00\mathscr{T}$, (*b*) $8.38\mathscr{T}$, (*c*) $8.63\mathscr{T}$, (*d*) $8.96\mathscr{T}$.

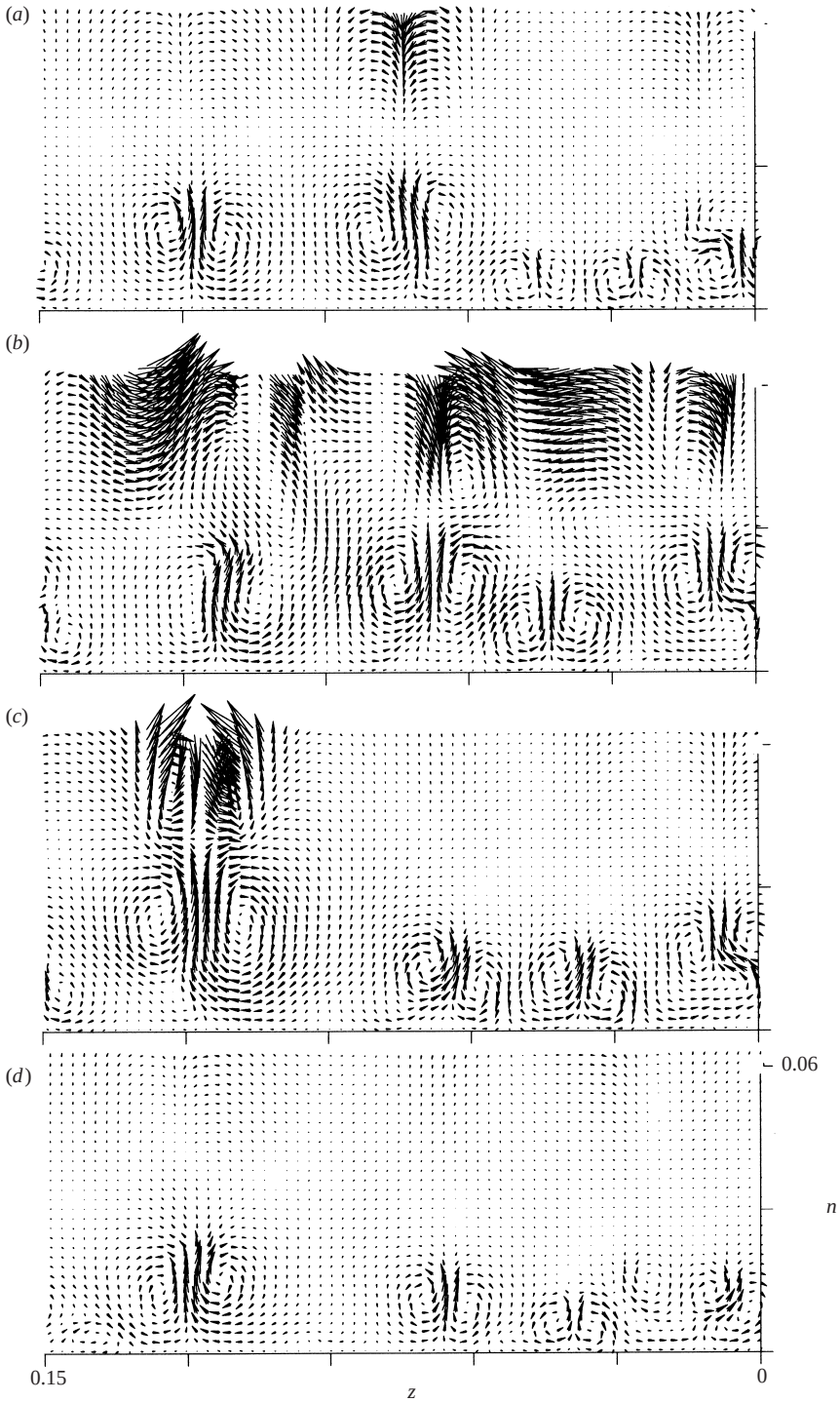

FIGURE 13 (*a–d*). For caption see facing page.

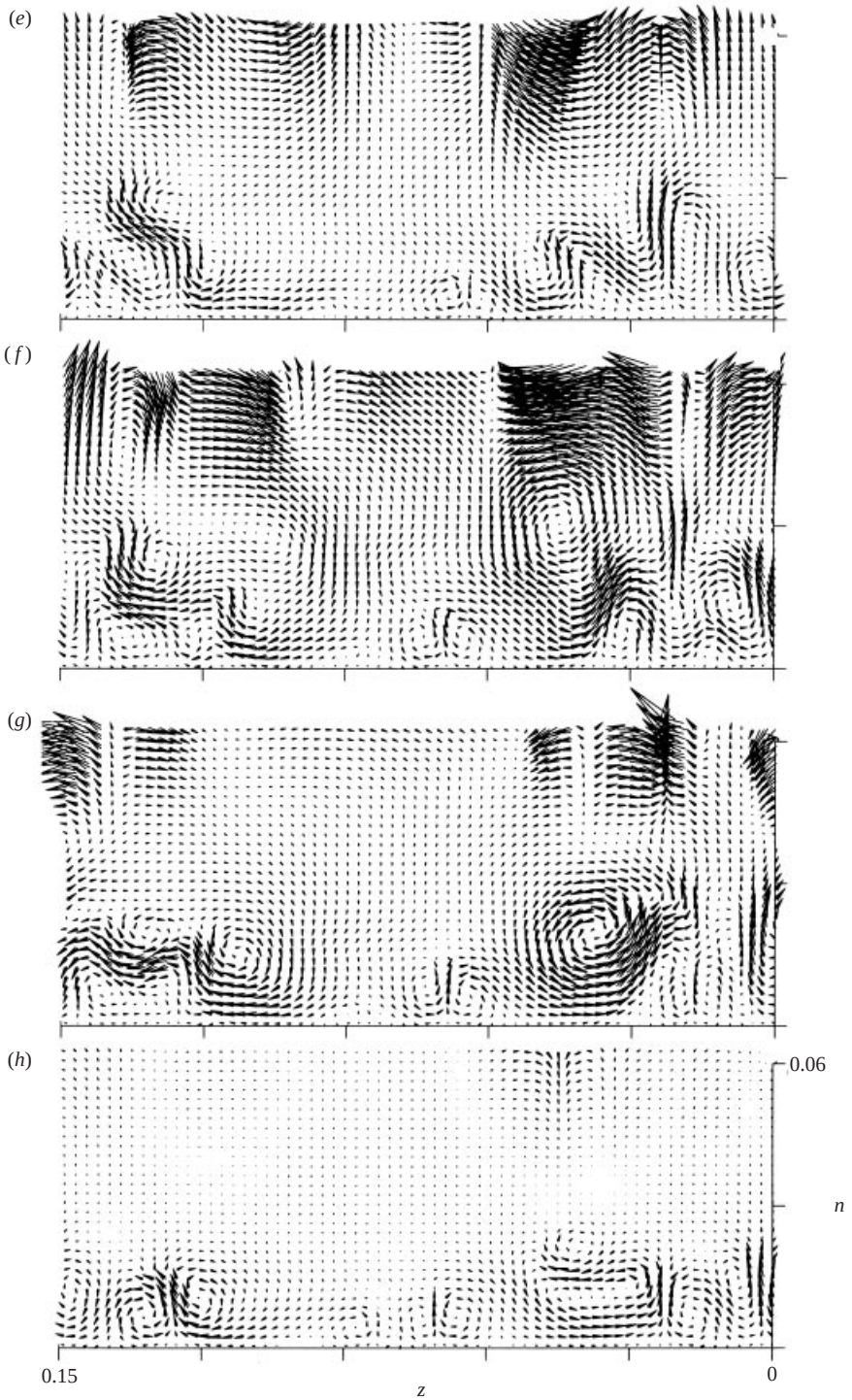

FIGURE 13. Fluctuating velocity vectors (spanwise-averaged mean subtracted) in the plane perpendicular to pressure surface at $x_w = 0.7$. (*a*) $t = 8.00\mathscr{T}$, (*b*) $8.38\mathscr{T}$, (*c*) $8.63\mathscr{T}$, (*d*) $8.96\mathscr{T}$, (*e*) $9.22\mathscr{T}$, (*f*) $9.43\mathscr{T}$, (*g*) $9.59\mathscr{T}$, (*h*) $10.00\mathscr{T}$.

details on the correlation between wake disturbance and development of the near-wall mushrooms can be easily extracted by comparing figure 12 and figure 13.

In figure 11, fluctuating velocity vectors away from the wall return to very small levels after the wakes pass. Disturbances from the passing wakes show up with distinct periodicity. This is unlike the disturbances shown in figure 12 and figure 13. Figure 13 shows the fluctuating velocity vectors at the same time coordinates as in figure 11, but now in the same plane as figure 12. Turning of the turbine passage is such that at $x_w = 0.7$ the pressure surface is nearly parallel to the stretched wakes (figure 8). The severely strained wakes manifest themselves in figure 8 in the form of a narrow band of high velocity fluctuation. In addition, wakes from different passing periods overlap with each other. Thus in figures 12 and 13 disturbances from the free-stream wakes are observed to be preset at nearly all of the eight instants. This is in stark contrast to the situation at $x_w = 0.3$, where the wake is present at only two of these times.

6. Vortices identified in three dimensions

We have argued that the pressure-side vortices are not Görtler vortices induced by instability of the concave boundary layer; rather they are most likely a forced response to the incident wake. So far the data presented are tantalizing, but difficult to assemble into a clear picture of the process. The most compelling evidence comes from three-dimensional visualization of the wake distortion. Producing such views raises the much debated question of how to identify a vortex. We have used both the $Q > 0$ and $\lambda_2 < 0$ techniques (Jeong & Hussain 1995), with similar results. For the figures in this section we have chosen to show zones of $\lambda_2 < 0$. λ_2 is the second largest eigenvalue of $\boldsymbol{S}^2 + \boldsymbol{\Omega}^2$, where $\boldsymbol{S}$ and $\boldsymbol{\Omega}$ are the symmetric and antisymmetric components of the velocity gradient tensor $\nabla \boldsymbol{u}$, respectively. Q is the second invariant of the velocity gradient tensor.

Figure 14 shows three-dimensional, perspective views of negative-λ_2 regions at three consecutive instants. The time span covers one full passing period from $8.00\mathscr{T}$ to $8.96\mathscr{T}$. Jeong & Hussain (1995) proposed that regions of negative λ_2 identify a vortex core. Before computing λ_2 for figure 14, the spanwise-averaged mean velocity was subtracted; hence these are vortices of the fluctuating field. λ_2 was also computed with the mean spanwise-averaged velocity being retained; the vortices identified from the total velocity and from the fluctuating velocity were almost identical.

Figure 14 shows that prior to entering the turbine passage the wake does not exhibit distinct vortical structures. Straining of the incoming wake starts to be applied near the stagnation point on the pressure side. As discussed in § 3, the local wake is stretched approximately along the x_{wake}-axis and compressed along y_{wake}. The consecutive time sequence plots in figure 14 follow the response of wake vortical structures to the straining.

Fluctuating vortex filaments in the upstream wake do not show a strong preferred orientation, and are close to random with respect to the principal axes of strain. They form a layer of vortices embedded in the mean wake. Stretching aligns the vortex filaments towards the axis of principal stress σ_1 and intensifies vorticity magnitude in that direction. Further stretching gradually collapses this layer of vortex filaments into circular tubes. This strained wake is much more complicated than in previous studies, but its initial response to stretching shows some broad similarities to cases studied in Sutera *et al.* (1963), Sadeh (1968), Keffer (1965) and Rogers (2000). Nevertheless, the nature of the initial response in the present flow is difficult to anticipate – even more so for the subsequent development and interaction with the wall.

As the cumulative effect of the rate of strain is felt, the circular tubes become progressively more distinct. They might be considered as leg elements of some extremely long hairpin vortices. The head of the hairpin is immersed inside the wake and not clearly visible, but it is needed in order for the vorticity to be solenoidal.

While we cannot offer a detailed analysis of the distortion process, the essential formative elements are those displayed in figures 4(*a*) and 4(*b*): reorientation by convection and mean straining. The turbine passage creates these elements in a concrete setting. It provides large total strains and an incident wake with its axis skewed to the flow direction. Flow gradients in the passage re-orient the wake axis. The further component of the turbine is the blade surface.

Note, again, that the legs away from the wall upstream of $x_w = 0.4$ are not parallel to the main flow. These free-stream legs constitute the primary longitudinal vortices. At the pressure surface the legs are dragged downstream with the migrating wake and flattened against the wall. The term 'longitudinal' is used loosely in this paper; the terminology is indicated in figure 1. Away from the pressure surface and upstream of $x_w = 0.4$, the 'longitudinal' vortex axis is not parallel to the main flow streamwise direction; it is approximately aligned with x_{wake} and with the direction of stretching. With the turning of the turbine, wakes are gradually rotated counterclockwisely, causing more and more of the leg to attach to the pressure surface. Thus the flattened primary vortices at the wall are continuously fed by the descending free-stream legs. Figure 14 also shows the dramatic degree of stretching and thinning of the primary vortices near the downstream half of the pressure surface. A dramatic difference between the pressure- and suction-side wakes is also evident. The latter are highly irregular, with a good deal of small-scale turbulence. The orientation of the wake approximately in the direction of negative rate of strain is responsible for this different evolution. Compression along the wake increases the velocity defect and intensifies turbulence.

In § 5, we observed in cross-section the engulfing of near-wall counter-rotating vortex pairs by a new passing wake. The process is visualized in three dimensions by figure 15. This figure shows regions of negative λ_2 within a wall-normal distance of 0.03 from the pressure surface. The flattened primary vortices and induced secondary vortices are inside this wall-normal range (figure 11). The three instants are the same as those in figure 14. In figure 15, grid lines from $x_w = 0.1$ to 0.9 are overlaid on the pressure surface. Compared to figure 14, in which the full passage is shown, figure 15 presents a more refined picture of the inception and development of streamwise vortices. In the figure, the round knob near the upstream end is where the free-stream leg is bent at the wall. Starting from figure 15(*a*), the dragging of the primary vortices is seen quite clearly by following the downstream convection and elongation of that knob structure through the set of temporal frames. The induction of an adjacent secondary streamwise vortex is also evident.

7. Time-averaged statistics

The focus of this paper is on the wake distortion. We will present only a few plots of statistical data. Without the previous flow visualizations some of these statistics would be mysterious. As it stands, they can be seen as signatures of the vortical features.

Figure 16 shows that the three r.m.s. velocity fluctuations peak at different normal distances. They are consistent with the velocity vector plots in figure 11: strong spanwise fluctuations occur at the bottom surface of the vortex, where the image

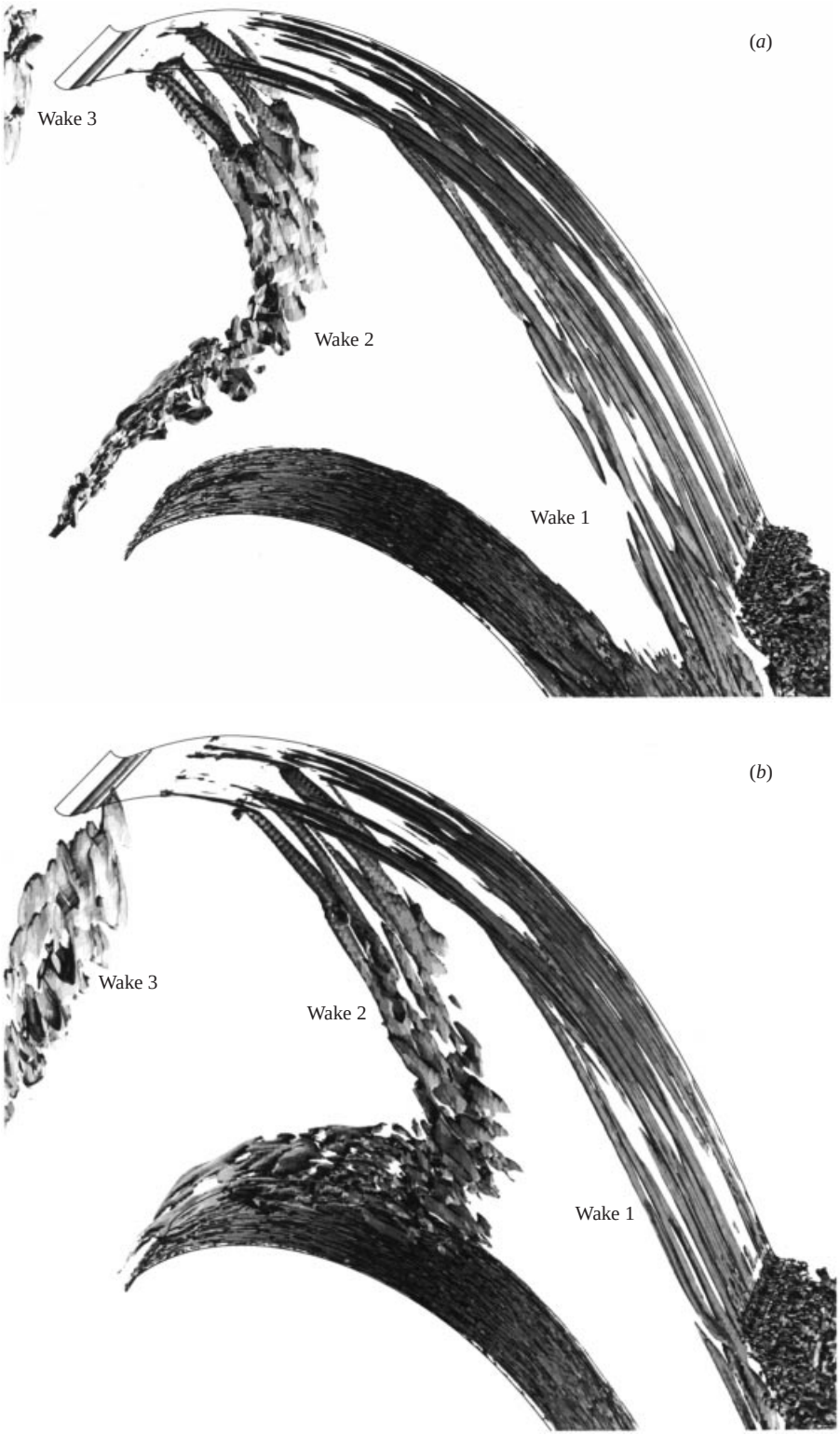

FIGURE 14 (*a*, *b*). For caption see facing page.

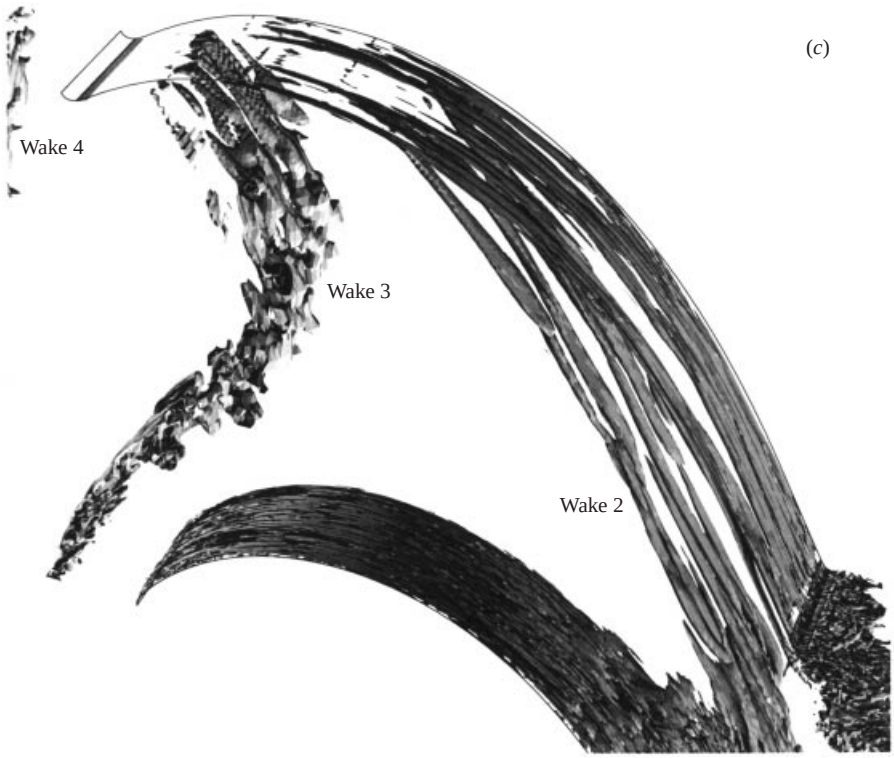

FIGURE 14. Regions of negative λ_2 inside the turbine passage. (*a*) $t = 8.00\mathscr{T}$, (*b*) $8.38\mathscr{T}$, (*c*) $8.96\mathscr{T}$.

effect enhances it (figure 11*c*); the largest wall-normal fluctuations occur at the central top surface of the vortex (tip of the mushroom); the peak streamwise fluctuation is found in between, also in the upwash region.

Profiles of the mean velocity component tangential to the pressure surface versus wall-normal distance are plotted in figure 17. Also shown are the velocities in the base flow, with no wake. Evidently, the effect of the longitudinal vortices on the mean flow is limited to within 3% of axial chord from the surface. That is consistent with earlier vector plots of the velocity field.

Profiles of spanwise velocity fluctuations $\overline{w'^2}$ are shown in figure 18. Most noticeable in the figure is the existence of a plateau in the two profiles at $x_w = 0.4$ and 0.5. The r.m.s. spanwise fluctuation in figure 16 also has a distinct plateau. This can be explained by comparing figure 11, at $x_w = 0.3$ to figure 13, at $x_w = 0.7$. At the upstream location, the near-wall vortices are modulated by free-stream passing wakes with distinct periodicity. Relatively large spanwise fluctuations are found near the top surface of the vortices. Beyond this surface, spanwise fluctuations drop rapidly with wall-normal distance, thus forming a plateau in the $\overline{w'^2}$ profiles. At the downstream location, after the flow is turned by the blade passage, free-stream spanwise fluctuations are present almost all of the time.

The turbulent intensity is plotted in figure 19. Wall-normal profiles of $\overline{u'^2} + \overline{v'^2} + \overline{w'^2}$ are provided at the same six streamwise stations as in the previous figure. The plateau is now in the profiles downstream of $x_w = 0.5$. This can be explained by comparing the less developed structures at $x_w = 0.3$ in figure 11(*h*) to the matured structures, also shown in figure 12. In figure 12 the round heads of the mushrooms form a region

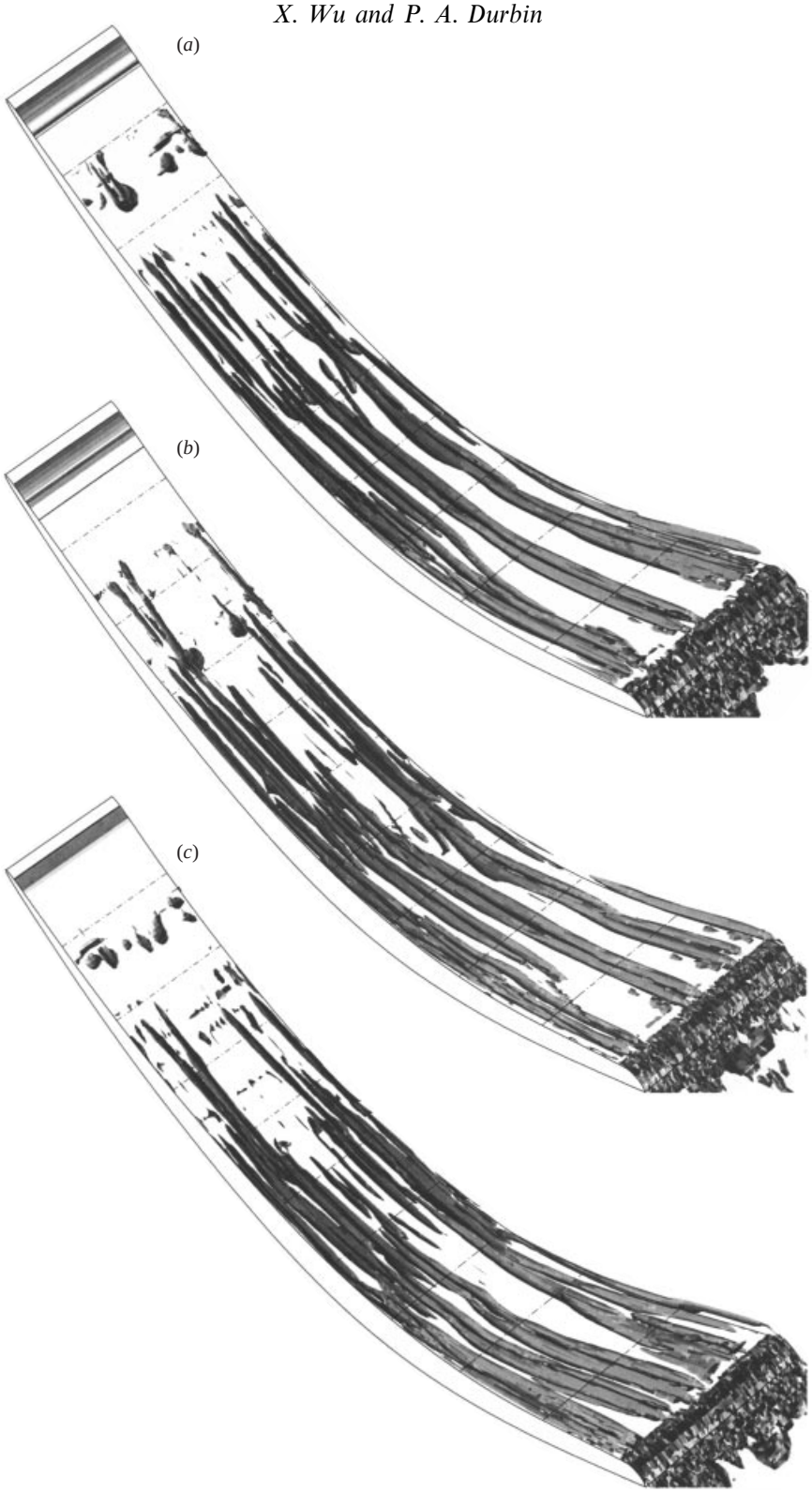

FIGURE 15. Regions of negative λ_2 near the pressure surface; —— marks $0.1 \leqslant x_{\text{wall}} \leqslant 0.9$ with increment 0.1. (*a*) $t = 8.00\mathscr{T}$, (*b*) $8.38\mathscr{T}$, (*c*) $8.96\mathscr{T}$.

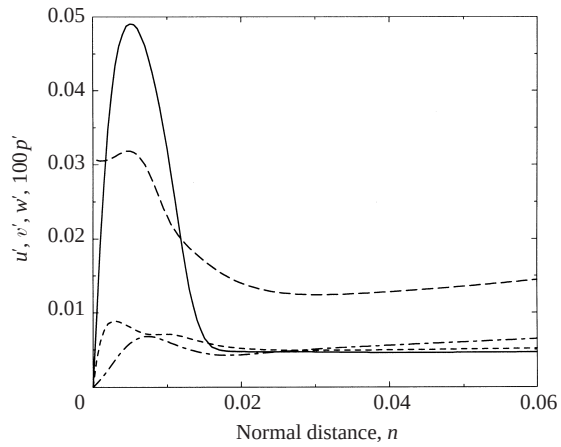

FIGURE 16. Time-averaged r.m.s. velocity and pressure fluctuations as functions of normal distance from the pressure surface at $x_w = 0.294$ (summit); ——, u'_{rms}; – – –, v'_{rms}; — — —, w'_{rms}; ——, $10^2 p'_{rms}$.

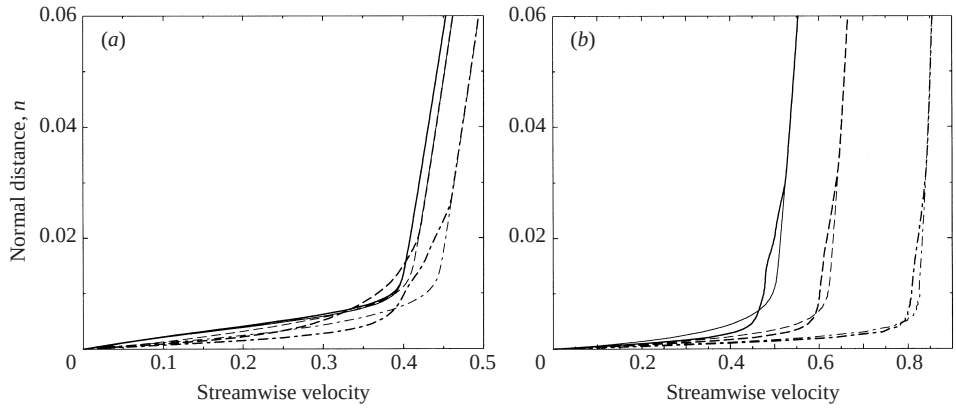

FIGURE 17. Time-averaged mean streamwise velocity (tangent to the pressure surface); thick lines: with wake; thin lines: no wake; (*a*) ——, $x_w = 0.2$; — — —, 0.4; – – –, 0.5; (*b*) ——, $x_w = 0.6$; — — —, 0.7; – – –, 0.8.

in which streamwise fluctuations are relatively large. Beyond the top surface of the mushrooms there is a rapid reduction in the magnitude of streamwise fluctuation with increasing wall-normal distance.

8. Concluding remarks

New phenomenon of fundamental fluid mechanical interest have emerged from these numerical simulations of migrating wake flow. A process was uncovered by which flow features descend from a passing wake and become near-wall features. When viewed in isolation, or within a single spanwise and wall-normal plane, surface longitudinal vortex pairs appear to show conventional signatures of Görtler vortices; however, they are not produced by a Görtler instability. The evidence presented herein is that they are a forced response to the incident wake. Their formation is preceded by a selective intensification of longitudinal vortices within the strained wakes. These vortices are then deposited onto the wall.

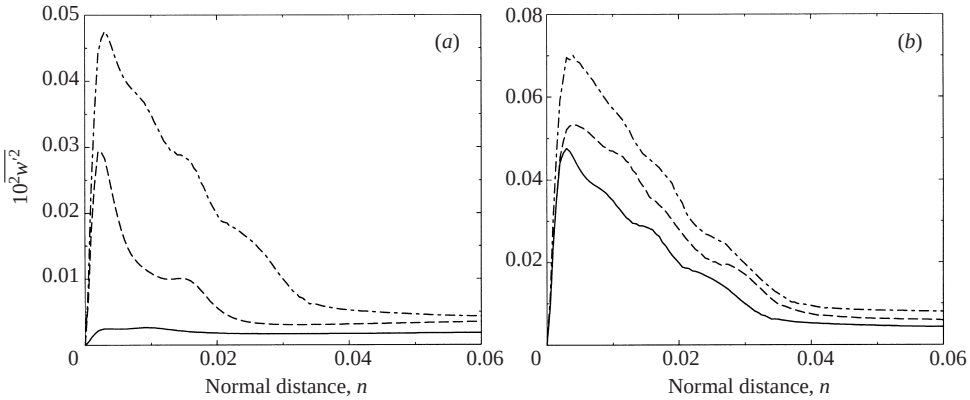

FIGURE 18. Time-averaged spanwise velocity fluctuations: (*a*) ——, $x_w = 0.2$; — —, 0.4; – – –, 0.5; (*b*) ——, $x_w = 0.6$; — —, 0.7; – – –, 0.8.

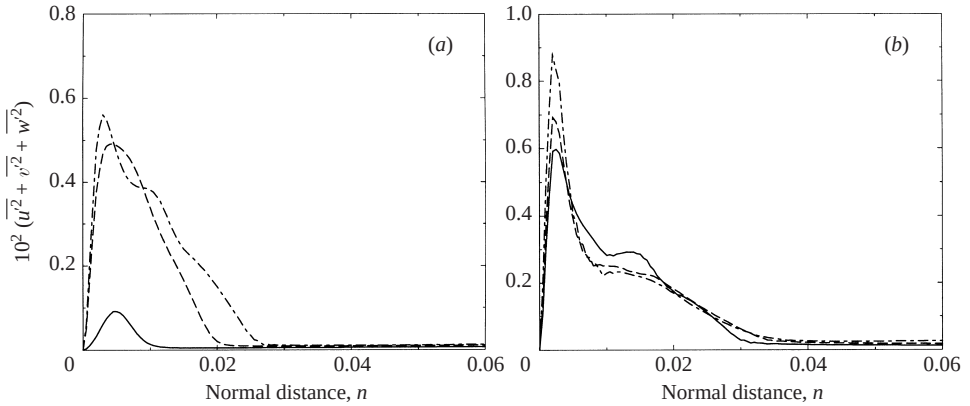

FIGURE 19. Profiles of $\overline{u'^2} + \overline{v'^2} + \overline{w'^2}$: (*a*) ——, $x_w = 0.2$; — —, 0.4; – – –, 0.5; (*b*) ——, $x_w = 0.6$; — —, 0.7; – – –, 0.8.

Sutera *et al.* (1963) described the process of vorticity amplification and vortex filament re-orientation by stretching round a blunt stagnation point. While there has been speculation that long vortices might similarly arise from turbulence wrapped around the leading edge of a turbine blade, the present simulations show how the vortices can emerge even in the middle of the passage. Indeed, stretching round the leading edge only influences the suction surface; but the selective amplification of longitudinal vortices is restricted to the vicinity of the pressure surface.

A substantial total strain evolves beyond the stagnation point on the pressure surface. At first, circular vortex tubes aligned in the direction of stretching emerge. These primary vortex tubes can be considered as leg elements of some sort of hairpin structure. The stretching initially is not parallel, but nearly transverse, to the local main flow direction.

Subsequent development and interaction with the wall is quite dramatic. The primary vortices are dragged downstream and flattened against the blade pressure-side surface. There they become streamwise vortices, parallel to the wall. Under the constraint of no-slip, secondary vortices are generated, with the opposite sense of rotation to the primary vortices; thus vortex pairs appear adjacent to the surface. As

they move downstream, these pairs tend to be engulfed by the structures laid down by the next passing wake.

Sharp turning of the turbine passage causes the free-stream vortices to descend towards the wall over the downstream half of the pressure side. By contrast, the wake wraps around the leading edge of the suction surface, but then travels above it. A bow forms between the pressure- and suction-side wakes. Spanwise vorticity of opposite signs accumulates at the apex of the bow, which becomes a region of intense turbulence.

The strong longitudinal vortices that form in the passing wake may have practical engineering importance. It is known that the turbine pressure surface can run hotter by as much as several hundred degrees Kelvin than the suction surface (Sharma & Stetson 1998). Of course, this is an issue in the high-pressure turbine, while the flow here is that of a low-pressure turbine; however, some of our observations may be relevant. Heat transfer enhancement by longitudinal vortices is discussed by Sutera *et al.* (1963). Intense streamwise vortices, descending from passing wakes, could play the same role, especially for the flow near the downstream half of the pressure surface.

This work is supported by the Academic Strategic Alliance Program of the U.S. Department of Energy Accelerated Strategic Computing Initiative. The computations were performed on the SGI Origin 2000s at the Advanced Computing Laboratory of Los Alamos National Laboratory.

REFERENCES

Duden, A., Raab, I. & Fottner, L. 1999 Controlling the secondary flow in a turbine cascade by three-dimensional airfoil design and endwall contouring. *ASME J. Turbomachinery* **121**, 191–199.

Engber, M. & Fottner, L. 1996 The effect of incoming wakes on boundary layer transition of a highly loaded turbine cascade. *Loss Mechanisms and Unsteady Flows in Turbomachines.* AGARD-CP-571.

Floryan, J. M. 1991 On the Görtler instability of boundary layers. *Prog. Aerospace Sci.* **28**, 235–271.

Hawthorne, W. R. & Novak, R. A. 1969 The aerodynamics of turbomachinery. *Ann. Rev. Fluid Mech.* **1**, 341–366.

Hodson, H. P. 1998 Blade row interactions in low pressure turbines. In *Blade Row Interference Effects in Axial Turbomachinery Stages* (ed. C. H. Sieverding & H. P. Hodson). Von Karman Institute for Fluid Dynamics Lecture Series 1998-02.

Hsu, K. & Lee, L. 1991 A numerical technique for two-dimensional grid generation with grid control at all of the boundaries. *J. Comput. Phys.* **96**, 451–469.

Jeong, J. & Hussain, F. 1995 On the identification of a vortex. *J. Fluid Mech.* **285**, 69–94.

Keffer, J. F. 1965 The uniform distortion of a turbulent wake. *J. Fluid Mech.* **22**, 135–159.

Kestin, J. & Wood, R. T. 1970 On the stability of two-dimensional stagnation flow. *J. Fluid Mech.* **44**, 461–479.

Kleiser, L. & Zang, T. 1991 Numerical simulation of transition in wall-bounded shear flows. *Ann. Rev. Fluid Mech.* **23**, 495–537.

Lee, K. & Liu, J. T. C. 1991 On the growth of mushroomlike structure in nonlinear spatially developing Görtler vortex flow. *Phys. Fluids* A **4**, 95–103.

Lin, S. J. & Corcos, G. M. 1984 The mixing layer: deterministic models of a turbulent flow. Part 3. The effect of plane strain on the dynamics of streamwise vortices. *J. Fluid Mech.* **141**, 139–178.

McCune, J. E. & Hawthorne, W. R. 1976 The effects of trailing vorticity on the flow through highly loaded cascades. *J. Fluid Mech.* **74**, 721–740.

Neu, J. C. 1984 The dynamics of stretched vortices. *J. Fluid Mech.* **143**, 253–276.

Rogers, M. M. 2000 The evolution of strained turbulent plane wakes. *J. Fluid Mech.* (submitted).

Rosenfeld, M. & Kwak, D. 1993 Multigrid acceleration of a fractional step solver in generalized curvilinear coordinate systems. *AIAA J.* **31**, 1792–1800.

Rosenfeld, M., Kwak, D. & Vinokur, M. 1991 A fractional step solution method for the unsteady incompressible Navier-Stokes equations in generalized coordinate systems. *J. Comput. Phys.* **94**, 102–137.

Sadeh, W. Z. 1966 An investigation of vorticity amplification in stagnation flow. PhD Thesis, Brown University.

Sharma, O. P. & Stetson, G. M. 1998 Impact of combustor generated temperature distortions on the performance, durability and structural integrity of turbines. In *Blade Row Interference Effects in Axial Turbomachinery Stages* (ed. C. H. Sieverding & H. P. Hodson). Von Karman Institute for Fluid Dynamics Lecture Series 1998-02.

Sutera, S. P., Maeder, P. F. & Kestin, J. 1963 On the sensitivity of heat transfer in the stagnation-point boundary layer to free-stream vorticity. *J. Fluid Mech* **16**, 497–520.

Weiss, A. P. & Fottner, L. 1995 The influence of load distribution on secondary flow in straight turbine cascades. *J. Turbomachinery* **117**, 133–141.

Wu, X. & Durbin, P. A. 2000*a* Numerical simulation of heat transfer in a transitional boundary layer with passing wakes. ASME *Trans. ASME: J. Heat Transfer* **122**, 248–257.

Wu, X. & Durbin, P. A. 2000*b* Boundary layer transition induced by periodic wakes. *J. Turbomachinery* **122**, 442–449.

Wu, X., Jacobs, R. G., Hunt, J. C. R. & Durbin, P. A. 1999 Simulation of boundary layer transition induced by periodically passing wakes. *J. Fluid Mech* **398**, 109–153.